

The diurnal cycle of clouds and precipitation along the Sierra Madre Occidental observed during NAME-2004: Implications for warm season precipitation estimation in complex terrain

STEPHEN W. NESBITT

Department of Atmospheric Sciences, University of Illinois at Urbana-Champaign, Urbana, Illinois

DAVID J. GOCHIS

Research Applications Program, National Center for Atmospheric Research, Boulder, Colorado*

TIMOTHY J. LANG

Department of Atmospheric Science, Colorado State University, Fort Collins, Colorado

Submitted to *J. Hydrometeorology*

7 June 2007

Revised

21 December 2007

Accepted

31 January 2008

*The National Center for Atmospheric Research is funded by the National Science Foundation.

Corresponding author address: Prof. Stephen W. Nesbitt, Department of Atmospheric Sciences, University of Illinois at Urbana-Champaign, 105 S. Gregory St., Urbana, IL 61801-3070.

E-mail: snesbitt@uiuc.edu

ABSTRACT

This study examines the spatial and temporal variability in the diurnal cycle of clouds and precipitation tied to topography within the North American Monsoon Experiment (NAME) Tier-1 domain during the 2004 NAME Enhanced Observing Period (EOP, July-August), with a focus on the implications for high resolution precipitation estimation within the core of the monsoon. Ground-based precipitation retrievals from the NAME Event Rain gauge Network (NERN) and CSU/NCAR version 2 radar composites over the southern NAME Tier-I domain are compared with satellite rainfall estimates from the CMORPH and PERSIANN operational and TRMM 3B42 research satellite estimates along the western slopes of the Sierra Madre Occidental (SMO). The rainfall estimates are examined alongside hourly images of high resolution GOES 11- μm brightness temperatures.

An abrupt shallow to deep convective transition is found over the SMO, with the development of shallow convective systems just before noon on average over the SMO high peaks, with deep convection not developing until after 15 LT on the SMO western slopes. This transition is shown to be contemporaneous with a relative underestimation/overestimation of precipitation during the period of shallow/deep convection from both IR and microwave precipitation algorithms due to changes in the depth and vigor shallow cloud and mixed-phase cloud depth. This characteristic life cycle in cloud structure and microphysics has important implications on ice scattering microwave and infrared precipitation estimates, and thus hydrological applications using high-resolution precipitation data, as well as the study of the dynamics of convective systems in complex terrain.

1. Introduction

Improving the basic understanding and model representation of warm season precipitation processes within the North American Monsoon System (NAMS) is a primary goal of the North American Monsoon Experiment (NAME; Higgins et al. 2006). Depending on location within the NAMS, summer rainfall in the monsoon region provides between 40-80% of the annual water resource (Douglas et al., 1993; Adams and Comrie 1997; Brito-Castillo, et al. 2003; Gochis et al. 2006) and, therefore, there is a pressing societal need for improved estimates of rainfall for water resources decision making and hydrological prediction activities. Previous work has shown that a primary mode of variability of precipitation within the core monsoon region exists on diurnal timescales (Negri et al. 1994; Gochis et al. 2003; 2004; 2007; Janowiak et al. 2005; Lang et al. 2007). However, the underlying mechanisms responsible for the diurnal variability in precipitation are often poorly represented in regional and global scale models simulating the NAMS (Gutzler et al. 2005). Since weather systems that modulate the intraseasonal variability of the monsoon (e.g. “gulf surges”, Bordoni and Stevens 2006; Bordoni et al. 2004; Stensrud et al. 1997) as well as moisture (Berbery 2001) and potential vorticity transports (Saleeby and Cotton 2004) influence convective processes across many scales, understanding various the modes and processes responsible for diurnally driven convective precipitation are critical to improving models and, thus, improving predictions of the NAMS.

The Sierra Madre Occidental (SMO) dominates the regional geography of the NAMS, extending from sea level to over 3000 m in elevation in several locations near the west coast of Mexico, containing deep canyon systems, steep slopes and high plateaus (Fig. 1) that greatly impact low- to mid-level atmospheric flow features in the region (Johnson et al. 2007). The SMO produces diurnally modulated upslope (downslope) flows during the day (night), thus exerting control on

moisture transport and convergence along the SMO mountain block (Berbery 2001). Given these factors, the initiation of convection is favored earlier in the diurnal cycle over high mountain peaks relative to the slopes or surrounding plains (Gochis et al. 2004), while total precipitation is maximized along the SMO western mid-slopes (see Fig. 1). The vertical structure and microphysical characteristics of midday developing convection over high terrain is of great interest since little is known about the details of precipitation frequency and intensity characteristics in the terrain of the SMO.

Once convection initiates in the high terrain of the SMO, it has been shown to occasionally grow upscale into Mesoscale Convective Systems (MCSs) that propagate towards the Gulf of California within the time-mean easterly flow (Farfan and Zehnder 1994; Janowiak et al. 2005; Lang et al. 2007). However, Lang et al. (2007) showed that there is significant intraseasonal variability in the degree to which convection organizes along the SMO and this variability influences precipitation production by convective systems of varying types within the diurnal cycle (Nesbitt and Zipser 2003). These important life cycle processes by which convection is initiated and grows upscale along the SMO must be better understood in order to be properly represented in numerical prediction models. The morphology of cloud and microphysical structures must also be well understood in order to develop confident estimates of precipitation from remote-sensing observation platforms. These needs underline the importance of a multi-scale approach to studying monsoon convective systems on diurnal to intra-seasonal time scales.

Since the operational precipitation observing network in northwest Mexico is not extensive or spatially dense, satellite observations are potentially a desirable tool to monitor occurrence and intensity structures in monsoon precipitation. However, biases in satellite precipitation estimates are only beginning to be explored in this region (e.g. Janowiak et al. 2005; Gebremichael et al.

2007; Hong et al. 2007), and are likely to be quite sensitive to the vertical structure of convection (Nesbitt et al. 2004; Fiorino and Smith 2006; Liu et al. 2007). Infrared-based techniques rely on the relationship between cloud-top temperature and surface rainfall (Xie and Arkin 1997; Sorooshian et al. 2000), while over-land passive microwave techniques currently rely on empirical relationships between 85-89 GHz ice scattering optical depth and surface precipitation (Ferraro 1997). Both of these techniques suffer when precipitation is shallow because the cloud top temperature is often too warm and there is often little or no cloud or precipitation ice to scatter radiation at these microwave frequencies.

Preliminary analyses show that convective clouds in the NAME region may have vertically varying structures as functions of topography (Hong et al. 2007; Rowe et al. 2008). This variability is hypothesized to cause biases in satellite-based rainfall estimates in the region. Therefore, characterization of uncertainties in satellite rainfall estimates within NAME may rely in large part on an understanding of the vertical profile of precipitation and cloud structures as functions of topography. Such an understanding is particularly important in the application of remotely sensed precipitation estimates for hydrological prediction in a region where strong gradients in precipitation character drive large differences in surface hydrological response (Vivoni et al. 2007). In this study, we will examine the diurnally evolving, vertical structure of clouds and other signatures of convection in an attempt to characterize the processes that control the diurnal cycle of clouds and precipitation behavior along the west slopes of the SMO.

This paper is organized in the following manner. In section 2, the data sources and data reduction are outlined. In section 3, we will discuss the differences in observed precipitation rates and frequencies in the region of interest. Sections 4 and 5 examine the varying convective vertical structures and microphysics as a function of elevation in the SMO, followed by

discussion and conclusions in sections 6 and 7.

2. Data

a. Ground-based precipitation measurements

Surface gauge measurements at 15-minute time resolution were obtained from the NAME Event Rain Gauge Network (NERN) from the National Center for Atmospheric Research (NCAR) Earth Observing Laboratory (EOL) during the period of the NAME EOP (1 July – 31 August 2004). Maintenance, calibration and data processing details of the NERN network are provided by Gochis et al. (2003; 2004; 2007). During the 2004 NAME EOP, the NERN consisted of 86 single, tipping bucket-type gauges distributed across six topographic transects shown in Fig. 1. Three scanning precipitation radars were operated from the period 7 July – 21 August 2004. These included two Servicio Meteorológico Nacional (SMN) C-Band operational Doppler radars located at Guasave and near Cabo San Lucas, as well as the NCAR S-Pol polarimetric radar near La Cruz de Elota (see Fig. 1 for the locations and nominal coverage areas of the radar data). Reflectivity data from these three radars were quality controlled and composited every 15 minutes (when available), and reflectivity and rain rate estimates were interpolated to a 0.05° lat-lon grid by Colorado State University and NCAR (Lang et al. 2007). This study uses the Version 2 of the CSU composites (Rowe et al. 2008), which features improved correction for beam blockage, hail contamination (using a 250 mm hr^{-1} cutoff), and use of polarimetrically tuned Z - R relationship ($Z = 133 R^{1.5}$) obtained using the methodology of Bringi et al. (2004). In the radar data, we have only analyzed locations in a particular hour with more than 90 accumulated scans over the entire experiment period. This limitation helps remove points which were only scanned intermittently (i.e. those points occurring only at far ranges due to changes in

the maximum range set for particular radars during the experiment).

b. Satellite data

Gridded 3-hourly 0.25° horizontal resolution satellite rainfall estimates were obtained from three sources: (1) CMORPH (NOAA Climate Prediction Center MORPHing technique); this technique advects precipitation estimates from the Special Sensor Microwave/Imager (SSM/I), Advanced Microwave Sounding Unit-B (AMSU-B) and Tropical Rainfall Measuring Mission (TRMM) passive microwave sensors in time using higher temporal resolution geostationary infrared (IR) data (Joyce et al. 2004). (2) PERSIANN (Precipitation Estimation from Remotely Sensed Information using Artificial Neural Networks); uses neural network classification/approximation procedures to compute an estimate of rainfall rate using geostationary IR brightness temperatures. The algorithm uses TRMM 2A12 passive microwave rainfall estimates as input into the neural network (Hsu et al. 1997; Sorooshian et al. 2000; Hong et al. 2005). Note that this study uses the operational version of PERSIANN, while a related study by Hong et al. (2007) uses a parallel version of PERSIANN with a cloud classification scheme (PERSIANN-CCS) which is described as using the measured IR brightness temperature characteristics to select a more appropriate microwave rain rate estimate (Hong et al. 2004). (3) TRMM 3B42 version 6 (hereafter 3B42); calibrates IR precipitation estimates with TRMM 2B31 combined radar and microwave estimates of precipitation, as well as other passive microwave satellites; monthly accumulations are adjusted to gauge accumulations over land (Huffman et al. 2001; Huffman et al. 2007).

To examine the vertical structure of convection as a function of the diurnal cycle, 4 km gridded, half-hourly, globally stitched IR brightness temperatures from geostationary satellites (Janowiak

et al. 2001) were obtained from the NOAA Climate Prediction Center via the NASA Goddard Space Flight Center Data and Acquisition Center for the period 1 July – 31 August 2004. These data were linearly interpolated to the 5 km grid of the CSU/NCAR radar composites described above.

3. Comparison of precipitation estimates

a. Comparison methodology

The first objective of this study is to compare the estimated diurnal cycles of precipitation frequency and intensity from the various precipitation products in the region. Each dataset was placed onto a common $0.25^\circ \times 0.25^\circ$ grid at 3-hourly time resolution for the reporting period 00 UTC 1 July to 21 UTC 31 August 2004. Note that the period of accumulation corresponding to each reporting time varies among the satellite estimates. For a reporting time of 12 UTC, for example, 3B42 reports estimated precipitation for the period 09:30 UTC to 11:30 UTC, while CMORPH and PERSIANN report precipitation from 12 UTC to 15 UTC. These datasets were kept in their native time resolution to avoid temporal interpolation errors, while radar and gauge data were interpolated to the 3B42 3-hr time bins. Radar (0.05°) and gauge (point) data were upscaled via linear interpolation (in boxes with at least 1 radar or gauge observation) to the same 0.25° grid. Once the precipitation estimates were combined, elevation data from 30-arc second (~ 1 km horizontal resolution) GTOPO30 terrain data from the United States Geological Survey were linearly interpolated to the same 0.25° grid, and over-land points were binned into three elevation bands: below 500 m (coastal plain), 500-2250 m (foothills), and above 2250 m (high peaks). Rain rates and precipitation frequencies were calculated based on accumulations or the number of 3-hourly periods with measurable precipitation divided by the total number of

observations, respectively (including rain and no rain periods).

Well-known uncertainty is present when comparing precipitation measurements from different platforms (e.g., from gauges, radars, and satellite estimates) due to spatial and temporal sampling differences, and retrieval errors (Tustison et al. 2001; 2003; Steiner and Smith 2004). In the results herein, the quantification of these uncertainties are left to future work as (1) the observation network was not designed to fully quantify the sub-pixel variability in satellite and radar measurements, including variations on very small scales in topography (Gembremichael et al. 2007), and (2) we are unaware of any standard method which exists to quantify such uncertainty. Both of these facts motivate future high-resolution gauge and disdrometer measurements to examine these uncertainties. Recent work by Rowe et al. (2008) indicates that the statistical distribution of rain rates is similar between the NERN gauge measurements and NAME radar composites; this argues that the spatial character of the sampling uncertainty from these measurements to a satellite pixel scale may be similar. Given these uncertainties, and the fact that we have a much more extensive observation network than operational precipitation analyses in NW Mexico, it is felt that the length and number of observations collected in NAME are able to capture the bulk differences in precipitation characteristics we aim to depict.

b. Precipitation estimate comparisons as a function of elevation

Figures 2 and 3 show the total time series and mean diurnal cycles, respectively, of estimated rainfall accumulations from the five precipitation datasets. From the rainfall time series presented in Fig 2, it is apparent that significant precipitation occurs nearly every day somewhere within the analysis domain, and there is a strong diurnal component to the variability in all of the precipitation time series. There is significant day-to-day variability in the amplitude of the

diurnal cycle of rain rates, particularly at low elevations. All estimates tend to show modest increasing values of maximum precipitation with decreasing elevation as shown previously by Gochis et al. (2007).

Comparisons of mean diurnal precipitation rates are shown in Fig. 3a (All times have been adjusted to Mountain Standard Time, e.g., UTC – 7). These diurnal averages were then subtracted from the time series shown in Fig. 2 for each day, and the ratio of the variance of the resultant time series (with the mean diurnal cycle removed) to the original time series is calculated, and then subtracted from one. This ratio represents the fraction of variance explained by the diurnal time series whose values are provided in Table 1. Along with a qualitative inspection of Fig. 2, the values of the fractional variance show that the diurnal cycle is indeed more regular at the higher elevations of the SMO (in both phase and magnitude) compared with the Coastal Plain region. Precipitation at lower elevations is more subject to a higher degree of intraseasonal variability as well as extreme events compared with higher elevations. These results are consistent with those of Gochis et al. (2004) and Lang et al. (2007), the latter study showing that the late night-early morning maximum in precipitation along the Coastal Plain is primarily due to organized convective systems (e.g. MCSs) that propagate westward off of the SMO, or propagate northwestward from their region of origin near Puerto Vallarta.

Figure 3 presents a similar result, displaying the phase-lagging of estimated diurnal precipitation rate (a) and frequency maximum (b) as elevation decreases (moving from top to bottom panels). In comparing the precipitation datasets, there are differences in the estimated amplitude and timing of the diurnal cycle in this region. At high elevations (Fig. 3a, top panel), the CMORPH and radar data have a precipitation rate and frequency peak in the early afternoon, with corresponding higher magnitudes in precipitation rate. However, peak rain rates in the NERN,

PERSIANN, and 3B42 products occur in the late afternoon. Over the middle elevation bin (Fig. 3a, middle panel), the timing of the precipitation rate peak centers on 1700 LT and is similar in phase among all of the datasets. The NERN and 3B42 products exhibit closely-agreeing precipitation rates throughout the day while CMORPH, PERSIANN, and radar estimates produce significantly higher precipitation rates. Over the coastal plain (Fig. 3a, lower panel), PERSIANN and CMORPH have much higher mean and peak diurnal amplitudes of estimated precipitation rate compared to the radar, 3B42, and NERN products. CMORPH also tend to estimate the hour of peak rain rate 1 bin earlier (1700 LT) than the other four products (2000 LT).

c. Understanding radar-gauge discrepancies

To investigate variations in estimated precipitation frequency from the radar composites and NERN (aside from the satellite estimates), we will examine these datasets at higher resolution to bypass possible errors due to upscaling these natively high resolution estimates to 0.25° grids. Fig. 4 shows maps depicting the spatial pattern the hourly frequency of occurrence (expressed in %) of nonzero precipitation from the original radar composite 5 km grid (shaded) and at each NERN gauge site (shaded circles) for hourly intervals between 1100 and 1600 LT. At high elevations, precipitation frequencies before noon are smaller than later in the diurnal cycle. Note that the radar composites depict precipitation initiating and occurring more than 16% of the time over selected terrain features, while only 1 gauge (near 26.2°N , 106.5°W) estimates precipitation more than 16% of the time. Overall, absolute differences are small between these radar and gauge estimates, and this likely explains why the precipitation frequencies in the 1100 LT bin in Fig. 3 over high elevations are small. Later, in the diurnal cycle over high terrain, precipitation frequencies are comparable (Fig. 3b), with a slight tendency for the NERN gauges to have higher

precipitation frequencies. This can also be seen the 1500 and 1600 LT panels of Fig. 4. Precipitation ends for the most part by 2300 LT (not shown) in the high terrain, although radar-estimated rainfall diminishes before NERN estimated rainfall.

1. ISSUES IN THE SMO HIGH TERRAIN

Disparities between the radar and gauge estimates at high elevation may be explained, in part, by the radar beam dimension as a function of terrain geometry. In the high peaks of the SMO, despite the radar beam being 150-200 km from the radar, the elevation of the beam center is not more than 1-2 km above the mountain peaks (assuming an elevation angle of 0.8° which was used for S-Pol rain mapping; the elevation angle for the Guasave radar varied between 0.5° and 1.5°). This fact allows the radar to detect relatively shallow precipitation over the high terrain compared to if the terrain were lower in elevation for a given the range to target. However, at 200 km range, the 1.0° (1.4°) beamwidth of S-Pol (Guasave) is more than 3.2 (4.5) km wide. Provided that precipitation early in the diurnal cycle is likely isolated in nature (i.e. not well organized), the rather large size of the radar beam would tend to smear echo over large distances, biasing radar-estimated precipitation frequencies high (but conditional rain rates low due to echo smearing) relative to gauges. Biases in inverting reflectivity to rain rate, bright band contamination, and beam altitude above the freezing level all contribute to the uncertainty in estimating precipitation from radars and comparing radars and rain gauges at far ranges (Smith and Krajewski 1991).

2. ISSUES IN THE SMO FOOTHILLS

Over the mid slopes of the SMO, radar-estimated precipitation frequencies and intensities are nearly twice that of the NERN gauge estimates. One factor that may contribute to this relative

difference between radar and gauges in the foothills is the fact that there are comparatively few gauges in these regions covered by the area where precipitation is shown to be most frequent by the radars, say at 1600 LT. This would tend to cause the gauges to underreport precipitation frequency (and amount) as represented by the larger domain covered by the radars. This factor probably combines with radar range effects (resolution and beam elevation above the terrain), leading to higher frequencies of precipitation over these regions. Combining the large vertical distance between the lowest elevation radar beam and the surface in this region and potential representativeness of the gauge locations likely tends to radar estimates of precipitation rate and frequency to be higher than gauges over the mid-slopes.

3. ISSUES IN THE COASTAL PLAIN

Over the coastal plain, the radars again tend to estimate precipitation frequency higher than the NERN gauges. One reason for this may be that the locations of the NERN gauges are not ideal for capturing the sea breeze convection depicted in the radar analysis. This behavior is depicted as the observed coast-parallel band of enhanced precipitation frequency just inland from the Gulf of California beginning around 12 LT. Based on the figure, none of the NERN stations appears to be located in the radar-determined preferred location for sea breeze precipitation. In addition, subcloud evaporation may be significant between the elevation of the lowest radar beam and the surface along the coastal plain, where sub-cloud relative humidity tends to be comparatively lower than at higher elevation (Rosenfeld and Ulbrich 2003). Low-end differences in sensitivity between precipitation estimates may also contribute. For instance, 0.254 mm of rain accumulation is required in order to register a tip in NERN gauges, which is equivalent to a radar echo of 12 dBZ using the Z-R relationship listed above. This sensitivity may be important since much of the precipitation over the coastal plain in the nighttime hours is in the form of light

stratiform rain from MCSs (Lang et al. 2007).

d. Further examination of the satellite estimates

In terms of estimated precipitation frequency, 3B42 has a similar time series compared with NERN, while the radar, PERSIANN, and CMORPH time series are somewhat higher in magnitude. Precipitation frequency estimates over the highest terrain (> 2250 m, Fig. 3b top panel) are quite similar between NERN and radar estimates while radar estimates of precipitation frequency are significantly higher than NERN over the mid and low elevations. The radar rainfall rate estimates in Fig. 3 tend to overestimate precipitation accumulation relative to the NERN gauges at all elevation bands in this region. The fact that precipitation frequency biases tend to follow in the same pattern as precipitation amount for these estimates shows that these algorithms tend to agree in terms of conditional precipitation rate (since total precipitation is the product of precipitation frequency and conditional rain rate). At these time and space scales at least, the discrepancies tend to be largely the result of precipitation occurrence being different among these estimates (with the radar, CMORPH and PERSIANN having a larger spatial coverage of precipitation than NERN and 3B42), however the scaling properties of rainfall from the satellite to gauge scale need to be better understood in order to make such comparisons more quantitative.

Studies have shown that microwave algorithms such as used in CMORPH (using the TRMM 2A12, NESDIS AMSU/B, and NESDIS SSM/I algorithms; Joyce et al. 2004) and PERSIANN (using TRMM 2A12) often overestimate precipitation in deep convective regimes (McCollum et al. 2002; Nesbitt et al. 2004). In this comparison, it appears a similar positive bias exists in the PERSIANN and CMORPH satellite products relative to the TRMM satellite and NERN gauge

products. Issues with the backward interpolation in time may cause the early development of precipitation in CMORPH at high elevation, where precipitation rapidly develops around noon LT (Janowiak et al. 2005), however this hypothesis needs further testing.

Note agreement between the NERN and 3B42 in both estimated precipitation frequency and amount, particularly at low elevations. The agreement in precipitation amount and frequency between NERN and 3B42 at low elevations is likely due to the fact that the version 6 product is gauge adjusted using reported monthly accumulations (Huffman et al. 2007), however the gauge analysis used in 3B42 only contains a few operational gauges on the coastal plain. Since no NERN (or other) gauges are used in the adjustment, this likely leads to the relative underestimate of 3B42 relative to the other estimates at higher elevations (especially relative to radar along the mid-slopes). The un-gauge adjusted version of 3B42 (3B42RT) has precipitation amounts more than twice those of the 3B42 version examined here (not shown), putting its peak afternoon accumulations greater than either PERSIANN or CMORPH. For the remainder of this paper, characteristics of the cloud systems within diurnal cycle will be investigated to help explain the disagreements in precipitation estimates found above.

4. Diurnally varying convective vertical structure along the SMO

a. Statistical evolution of IR-inferred cloud structure along the SMO

As evidenced by the diurnally averaged precipitation time series in the previous section, rainfall often begins falling on the high elevation region of the SMO before local noon. However, as shown in Fig. 3, the 3B42 and PERSIANN combined infrared and microwave precipitation estimation techniques tend to somewhat underestimate precipitation rates compared with NERN observations during this period. In examining a different version of the PERSIANN algorithm

(the PERSIAN-Cloud Classification Scheme or -CCS), Hong et al. (2007) hypothesized that underestimation by microwave-adjusted algorithms early in the diurnal cycle may be due to the shallowness of the precipitating clouds during this time period. Over-land microwave retrievals rely on ice scattering techniques at 85 GHz (Ferraro 1997; Kummerow et al. 2001), precipitation without significant ice (i.e. with no or decreased mixed-phase microphysical processes occurring) will cause an underestimate such retrievals. This lack of sensitivity will at times cause a low bias in the relationship between both IR and microwave brightness temperatures and rainfall.

This leads us to the question; *does shallow precipitation exist over these high elevation regions early in the diurnal cycle* and, therefore lead to an underestimate in precipitation from IR and microwave algorithms? To examine this issue, IR brightness temperature images matched to the radar composite grid are examined to characterize the diurnal variability in the estimated height of clouds in this region. In Fig. 5, the percentage of time that an IR brightness temperature pixel reaches below 275 K is shaded, while the percentage of time pixels reached a threshold of 208 K is contoured in white. For reference, the 2250 m elevation contour is contoured in black. The 275 K threshold is selected to highlight convection reaching close to the freezing level, while the 208 K threshold is selected to highlight convection reaching near the tropopause. Note that according to the mean sounding at Mazatlán, calculated from all July and August sounding launches during 2004, 275 K corresponds to a mean height of 4.6 km, while 208 K occurred at 13.0 km. The time-mean tropopause (identified as the mean height at which a minimum temperature was identified) was slightly colder at 195 K and was located at 15.4 km altitude.

After reaching a minima in cloud cover around 09 LT, the frequency of occurrence of brightness temperatures < 275 K begins to increase over the highest terrain around 11 LT, indicating the

development of new convection; these clouds rapidly produce radar echos and precipitation (Fig. 4). This time of initiation corresponds well with convective initiation times in the Colorado Rockies reported by Banta and Schaaf (1987). Note that at 11 and 13 LT, no areas contain cloud top brightness temperature < 208 K more than 4% of the time, and the same is true at 235 K (not shown) except for one small region near Cerro Mohinora (elevation 3250 m near 26°N , 107°W). It is not until 15 LT that deep convection meeting the 208 K threshold exists in any region more than 4% of the time, and this occurs almost exclusively in the SMO western slopes below 2250 m elevation. The fact that the 208 K contours do not encroach on the high terrain (> 2250 m) indicates that convection rarely is of tropopause depth at these high elevations, even though it is common for shallow convection to be located in such locations ($\geq 64\%$ of the time).

After 15 LT, near-tropopause depth convection is very common over the western slopes of the SMO, tending, in most part, to die out by the time it reaches the Gulf of California coast by local midnight, except (1) along the northern extent of the analysis domain where 208 K frequency contours persist until approximately 3 LT, and (2) the large region of 208 K frequency contours to the south of Mazatlán towards Puerto Vallarta. Organized deep convection occasionally persists offshore through the night and into the next morning (Lang et al. 2007). Cloudiness trends tend to decrease at both brightness temperature thresholds throughout the morning, until the diurnal cycle re-initiates with new convection again by 11 LT. Thus, while the SMO-perpendicular diurnal cycle of convection can be largely represented as a symmetric composite, there is significant along-range variability to the diurnal cycle from areas where convection can last into the night and into the next morning.

To investigate this behavior in more detail, Fig. 6 shows the hourly evolution of the diurnal cycle of IR brightness temperature. Shading in Figure 6 indicates the relative fraction of IR brightness

temperature counts (only for observations ≤ 275 K to remove possible surface contamination) in 5 K brightness temperature bins as a function of each hour local time. At high elevations (Fig. 6a), there is a high fractional occurrence (> 0.7) of clouds in the bins with brightness temperature warmer than 265 K during 2 time periods: one centered on 09 LT and one centered on local noon. The former maximum (see also Fig. 5, 07-09 LT) could be due to two factors. Dissipating cirrus anvils from the previous day's convection, represented by the gradual slope of relative frequency contours towards warmer brightness temperatures in the evening and overnight hours, is consistent with gradually falling/sublimating ice crystals produced by the previous day's convection. Xie et al. (2005) noted a 'flat tail' to the IR brightness temperature distribution near the SMO crest, and attributed it to optically thin cirrus clouds. However, at high elevations low level stratus/ground fog was repeatedly documented on servicing trips to NERN gauges as well as in Alcantara et al. (2002). Nighttime cloud cover over the high terrain is important in determining radiative fluxes in the region, as well as influence the strength of radiatively-driven nocturnal downslope flows (Whiteman 2000). Since downslope flows are necessarily dry, nocturnal downslope flows could exhibit a strong influence the moisture availability at high terrain and along the SMO slopes, influencing conditions for the next day's convection (Ciesielski and Johnson 2008).

The latter maximum around local noon at high elevations (Fig. 6a) is the developing shallow convection along and just west of the SMO peaks. However, noting the dearth of deep cloudiness over the high elevations until well after noon, much of the cold cloudiness (< 220 K) may actually be eastwardly expanding anvils from convection, whose updrafts are actually to the west at lower elevations. In the foothills (middle panel), there is evidence of shallow cloud development around noon (with brightness temperatures > 265 K). However, the primary feature

of note is the high relative fraction of deep cold cloud (with temperatures < 210 K) present by mid-afternoon. Deep cloudiness is the prominent feature near and just after sunset over low elevation regions (right panel). There is a relative maximum of pixels with cold clouds < 200 K between 18 and 21 LT and a transition to warmer brightness temperatures thereafter, which is consistent with gradually dissipating cirrus anvils overnight.

b. Case study of diurnal evolution along the SMO

Fig. 7 illustrates a case study showing observed IR brightness temperatures and radar reflectivity composites every 4 hours from 2 August 2004 at 12 LT to 16 LT on 3 August 2004. By 12 LT 8/2, isolated convection developed over the high terrain of the SMO, with the cloud temperatures in this region ranging from 240 to 260 K – these are temperatures too cold to be associated with the surface. Note the striated appearance of the IR brightness temperatures on the eastern (upwind) side of the SMO, indicating the breakup of this warm cloud top feature (possibly via the development of convective rolls with solar heating and/or an upslope flow component). These circulations formed perpendicular to the east southeasterly SMO ridge-parallel flow depicted by the North American Regional Reanalysis (Mesinger et al. 2006) at this time (not shown).

Radar echoes are apparent along and just west of the high SMO terrain by 12 LT, and the NERN gauge stations at La Ermita (23.67°N , 105.72°W , 2716 m) and Las Rusias (23.74°N , 105.53°W , 2896 m) reported light precipitation (~ 1 mm) during the period 11-12 LT. During the next four hours, the convection organized and moved westward down the western SMO slopes (with IR brightness temperature minima falling in the range of 204-220 K). Note that during this afternoon period, convective and stratiform precipitation propagated westward, but the cold anvil

spread eastward back over the high terrain (this depicts the cause of late afternoon cold cloud tops at high elevations in Fig. 6 even though precipitation has moved to lower elevations). By 00 LT 8/3, most echo dissipated associated with the previous day's convection, and cloud top temperatures warmed in the remnants of this convection over the higher terrain and coastal plain. However, a pair of mesoscale convective systems which formed to the southeast of the domain moved northwest into the domain during the next morning. The aggregate of these type of systems is responsible for the enhanced probabilities for cold brightness temperatures offshore near the mouth of the Gulf of California during the early morning hours shown in Fig. 5.

Also, note by 04 and 08 LT the depiction of low-level (warm IR brightness temperature) stratus clouds over the high terrain (indicated with the white arrows in Fig. 7). These stratus clouds appear to break up into the roll-type circulations (and associated precipitation) that were evident over the SMO slopes the previous day at the same time (12 LT). Despite the presence of the mesoscale convective system near the Gulf of California shoreline on this day, convection at the higher elevations seemed to appear to form and organize in a similar fashion on 8/3 compared with 8/2 (e.g. near 24°N, 106°W) apart from areas where solar radiation is shaded at the surface by the MCS anvil. Thus, as was observed during the field campaign, the daytime orographically forced convection existed simultaneously with organized, propagating convection at lower elevations.

5. Convective environments along the SMO

To interpret differences in the convective low-level environments forcing cloud systems of different cloud top heights along the SMO, data from recording surface temperature and humidity sensors deployed by Art Douglas at Creighton University within instrument shelters at

the NERN gauge sites at La Cienega de Nuestra Señora near the SMO crest (25.0°N 106.3°W, elevation 2483 m), El Palmito (23.6°N, 105.8°W, elevation 1925 m), Mazatlán (23.2°N 106.4°W elevation 2 m), and Culiacán (24.8°N 107.4°W, elevation 66 m) were analyzed. Figure 8 shows the mean diurnal values (at half-hour increments) of temperature, relative humidity, and estimated cloud base height¹ at each site. Temperatures at La Cienega and El Palmito are much cooler than those at Mazatlán and Culiacán due to elevation effects. As temperatures rapidly rise at La Cienega following sunrise, near-saturated surface conditions are quickly mixed out, on average, over a period of approximately two hours. At El Palmito (~600 m below), temperatures rise more slowly (from pre-sunrise relative humidity values exceeding 90%), and over the coastal plain, diurnal heating occurs much more gradually (and mean nighttime relative humidities are < 90%). The observed trend of slowing of diurnal warming with decreasing elevation could be due to factors such as short wave or long wave radiative effects of increasing boundary layer specific humidity and evapotranspiration (Durre and Wallace 2001), or cool sea-breeze flows, particularly at Mazatlán (Ciesielski and Johnson 2008). Note that the mean diurnal maximum surface mixing ratio at La Cienega is 12.5 g kg⁻¹, while at Mazatlán it nears 20.3 g kg⁻¹. Afternoon minimum relative humidity values range along the coastal plain from roughly 70% at Mazatlán (very close to the Gulf of California) to less than 50% at Culiacán (in the central Coastal Plain). At the time when precipitating convection starts over the elevated terrain (11 LT), estimated cloud base heights are less than 1.0 km above ground level (AGL). At Culiacán they extend over 2 km AGL at the time of convective initiation.

These environmental conditions have several key impacts on precipitating cumulus convection in

¹ Cloud base height (in km) is calculated from Stull (1995) as $CBH = .125(T - T_d)$.

the SMO. First, the efficiency of warm rain processes in the convection that occurs at high elevations, with cloud base near the surface, will have reduced evaporation and thus increased precipitation efficiency compared to low elevation regions (Fig. 8b). Over the coastal plain and foothills, it is presumed (based on our limited measurements) that significant evaporation exists given that mean afternoon relative humidities are near 50%.

Second, convection over the high terrain is shown to be comparatively shallow (i.e. it is rarely tropopause-depth) with minimum cloud top IR brightness temperatures of 240-220 K (Fig. 6a), and CMORPH and PERSIANN satellite estimates have a delayed precipitation onset and less of an overall positive fractional bias compared with lower elevations (Hong et al. 2007). The lack of moisture available at cloud base in the high terrain relative to lower elevations (almost one-half the moisture in terms of specific humidity) likely limits the observed maximum height of convection since significantly less convective available potential energy (CAPE) and moisture (i.e. supercooled water) is available for latent heat release in convection. We hypothesize that for these reasons, the lack of moisture limits the vertical extent of convection at high elevations, and leads to a low bias in IR rainfall retrievals in such locations. This effect will also reduce, on average, the depth and intensity of mixed phase microphysical processes, reducing passive microwave ice scattering, and leading to an underdetection and low bias from microwave precipitation retrievals in elevated terrain where IR retrievals have a low bias.

Over the coastal plain, high adiabatic liquid water contents are hypothesized to lead to very intense tropopause-penetrating convective updrafts (Figs. 5 and 6) that produce copious precipitation-sized ice particles aloft, and strong depressions in IR and microwave brightness temperatures. Since the low levels of the atmosphere along the coastal plain typically have lower relative humidities than higher elevations (Fig. 11); sub-cloud evaporation is thought to decrease

surface rainfall as a function of microwave ice scattering. In addition, warm rain processes may be very efficient (despite mean cloud bases 1.25-2 km) along the coastal plain due to the large vertical distance between cloud base and the freezing level where warm microphysical growth can occur (Rowe et al. 2008). All of these factors are hypothesized to lead to positive biases in current infrared and microwave precipitation retrieval techniques.

6. Summary

A conceptual figure illustrating the hypothesized monsoon-averaged diurnal convective regime along the SMO is shown in Fig. 9. By local noon, relatively shallow and rapidly precipitating convection is triggered near the high peaks of the SMO. This convection has cloud base near the SMO peaks and has relatively little moisture available at its disposal (Fig. 11b). While propagating westward during the early afternoon, the convection remains shallow for 3 to 4 hours before it extends to tropopause depth in the SMO foothills by 15 LT. It is hypothesized that this time delay in the onset of deep convection along the SMO corresponds with the time within the diurnal cycle that it takes the convection to propagate downslope to locations with sufficient moisture – and thus convective available potential energy (CAPE) – to penetrate the tropopause. Shallow convection at high elevations will have warm IR brightness temperatures, which are less likely to trigger significant precipitation in infrared-based rainfall estimates, since these methods either use hard thresholds (e.g., the GOES Precipitation Index, Arkin and Meisner (1987)), derived linear relationships between surface precipitation accumulation and IR brightness temperatures (e.g. as in the 3B42 algorithm (Huffman et al. 2001; Huffman et al. 2007)), or neural-network matchups between microwave-estimated precipitation and IR brightness temperatures as is used by PERSIANN (Hsu et al. 1997; Sorooshian et al. 2000). Compared with the deeper convection observed later in the day, shallow convection located in

high terrain will more likely:

(1) have weaker mean updraft speeds that are less able to penetrate through the depth of the troposphere,

(2) produce a shallower depth of precipitation-sized ice, or exist completely below the freezing level and thus constitute a complete warm rain process that will scatter proportionally less 85 GHz microwave radiation out of the footprint,

(3) have lower total liquid water contents available since the lifted parcel is originating at a high altitude (>2250 m). This in turn will limit latent heat release and the vigor and/or depth of mixed phase microphysical processes, and

(4) be of smaller horizontal scale (i.e. less organized) as a result of weaker convective circulations, weaker cold pool dynamics, as well as increased entrainment. These processes will likely increase non-uniform beamfilling effects (Harris et al. 2003; Kummerow 1998) within the footprint of a microwave sensor (5×7 km in the case of TMI).

These factors likely lead to less ice scattering at 85 GHz for a given surface rain rate, and perhaps lead to decreased detectability of precipitation by current microwave methods over the high terrain of the SMO. Combined with IR underdetection of surface precipitation in shallow cloud regimes, and even potential spaceborne radar beamfilling, ground clutter, and side lobe contamination in such clouds, this underdetection problem likely compounds problems in remote sensing retrievals, resulting in an estimate of delayed onset and reduced intensities of precipitating systems over complex terrain.

Large differences in total precipitation amount exist among the estimates examined in these studies, and separating biases from sampling and representativeness errors requires development

of improved quantitative means of comparing precipitation measurements of different spatial and temporal resolutions (Tustison et al. 2001; 2003). Uncertainties in the scaling properties of rainfall will have significant implications in using spaceborne precipitation estimates as input into hydrologic prediction models. Understanding the uncertainties involved in determining the scaling properties of rainfall, both from observational and theoretical approaches, should be of key importance, since it is currently a scientific barrier in comparing rainfall data. Observing the properties of rainfall (rain rate, particle size distribution) at many sites at sub-satellite and radar pixel time and space scales would be one approach to addressing such importance scale issues.

A key question for future research is to determine the processes by which the shallow to deep, organized diurnal convective transition occurs along the SMO, including the roles of boundary layer structure and moisture transport within topographic flows. The organizational mechanism for these systems along the SMO slopes has yet to be attributed, but its characteristics appear to be similar to a slope flow MCS-generation mechanism (Tripoli and Cotton 1989a, b). These rainfall events have significantly higher intraseasonal variability than events in the foothills, likely due to variations in environmental flow, and moisture availability, convective instability, and “gulf surges” (Stensrud et al. 1997) need to be examined in close context with the life cycle of orogenically forced MCSs in the core monsoon region.

In addition, stratus and fog is commonly observed overnight in the high terrain, which likely plays an important role in the radiation balance over the SMO. We hypothesize that nocturnal clouds could limit radiational cooling and potentially limit nocturnal downslope flows, allowing moisture to persist along the slopes rather than be swept to lower elevations overnight by such flows, remaining to invigorate the next day’s convection once the stratus deck is broken. Evaporation of canopy and surface soil moisture may also provide accessible reserves for

feeding boundary layer moisture the following day (Durre and Wallace 2001). Given the relatively complex evolution of the diurnal cycle of convection, its forcing, and vertical structure, it is not surprising that convection-parameterizing models representing these process have significant difficulty representing the timing, intensity, and structure of precipitation and surface hydrology in the region (Gochis et al. 2002; 2003 and Gutzler et al. 2005). Therefore, continued collection and analysis of meteorological (including state parameter and cloud microphysical) alongside land surface datasets will be essential to improving our understanding and resolving deficiencies in warm season convection initiating and evolving from complex terrain.

Acknowledgements. Thanks go to Rob Cifelli, Steve Rutledge, Dave Ahijevych, Rit Carbone Paul Ciesielski, Bob Maddox, Art Douglas, and Bob Joyce for fruitful scientific discussions. The comments of four anonymous reviewers were very helpful. We wish to thank the staff of NCAR EOL for maintaining, operating, and collecting data from the NAME radars and Christopher Watts, Jaime Garatuza-Payán, Julio César-Rodríguez, and the Comisión Nacional del Agua of Mexico for continued collection and maintenance of the NERN stations. NERN, radiosonde, radar, surface, and lightning data were obtained from the NAME data archive at NCAR Earth Observing Laboratory, Boulder, CO (<http://www.eol.ucar.edu>). IR satellite data were obtained from NOAA Climate Diagnostic Center, Camp Springs, MD via the NASA Goddard Earth Sciences Data and Information Services Center, Greenbelt, MD (<http://daac.gsfc.nasa.gov>). Data analysis, NERN data collection and analysis, data collection from the SMN radars and creation of the radar composites is provided by the NOAA Climate Prediction Program for the Americas (CPPA) under Drs. Jin Huang and Annarita Mariotti (grants NA07OAR4310214 to SN, NA04OAR4310166 to DG, and NA04OAR4310153 to TL); the deployment of the S-Pol radar was funded by NSF grant ATM-0340544 to CSU and NCAR.

REFERENCES

- Adams, D. K. and A. C. Comrie, 1997: The North American monsoon. *Bull. Am. Meteorol. Soc.*, **78**, 2197-2213.
- Alcantara, A. O., I. Luna and A. Velaquez, 2002: Altitudinal distribution patterns of Mexican cloud forests based upon preferential characteristic genera. *Plant Ecol.*, **161**, 167-174.
- Arkin, P. A. and B. N. Meisner, 1987: The relationship between large-scale convective rainfall and cold cloud over the western-hemisphere during 1982-84. *Mon. Weather Rev.*, **115**, 51-74.
- Banta, R. M. and C. B. Schaaf, 1987: Thunderstorm genesis zones in the Colorado Rocky Mountains as determined by traceback of geosynchronous satellite images, *Mon. Weather Rev.*, **115**, 463-476.
- Berbery, E. H., 2001: Mesoscale moisture analysis of the North American monsoon. *J. Climate*, **14**, 121-137.
- Bordoni, S. and B. Stevens, 2006: Principal component analysis of the summertime winds over the Gulf of California. A gulf surge index, *Mon. Wea. Rev.*, **134**, 3395-3414.
- Bordoni, S., P. E. Ciesielski, R. H. Johnson, B. D. McNoldy and B. Stevens, 2004: The low-level circulation of the north American monsoon as revealed by QuikSCAT. *Geophys. Res. Lett.*, **31**, L10109.
- Brito-Castillo, L. A.V. Douglas, A. Leyva-Contreras, and D. Lluch-Belda, 2003: The effect of large-scale circulation on precipitation and streamflow in the Gulf of California watershed. *Int. J. Climatol.*, **23**, 751-768.

- Bringi, V. N., T. W. Tang and V. Chandrasekar, 2004: Evaluation of a new polarimetrically based Z-R relation. *J. Atmos. Ocean. Technol.*, **21**, 612-623.
- Ciesielski, P. E., and R. H. Johnson, 2008: Diurnal cycle of surface flows during 2004 NAME and comparison to model reanalysis. *J. Climate*, submitted.
- Douglas, M., R.A. Maddox, K. Howard, and S. Reyes, 1993: The Mexican Monsoon. *J. Climate*, **6**, 1655-1667.
- Durre, I., and J.M. Wallace, 2001: The warm Season dip in diurnal temperature range over the Eastern United States. *J. Climate*, **14**, 354-360.
- Farfan, L. M. and J. A. Zehnder, 1994: Moving and stationary mesoscale convective systems over northwest Mexico during the Southwest Area Monsoon Project. *Wea. Forecasting*, **9**, 630-639.
- Ferraro, R. R., 1997: Special sensor microwave imager derived global rainfall estimates for climatological applications. *J. Geophys. Res.*, **102**, 16715-16735.
- Fiorino, S. T. and E. A. Smith, 2006: Critical assessment of microphysical assumptions within TRMM radiometer rain profile algorithm using satellite, aircraft, and surface datasets from KWAJEX. *J. Appl. Meteor. Climat.*, **45**, 754-786.
- Gebremichael, M., E. Vivoni, C.J. Watts and J.C. Rodriguez, 2007: Submesoscale spatiotemporal variability of North American Monsoon rainfall over complex terrain. *J. Climate*, **20**, 1751-1773.
- Gochis, D.J., C.J. Watts, J. Garatuza-Payan, and J.C. Rodriguez 2007: Spatial and temporal

- patterns of precipitation intensity as observed by the NAME event rain gauge network from 2002 to 2004. *J. Climate*, **20**, 1734-1750.
- Gochis, D.J., L. Brito-Castillo, and W.J. Shuttleworth, 2006: Hydroclimatology of the North American Monsoon region in northwest Mexico. *J. Hydrol.*, **316**, 53-70.
- Gochis, D. J., A. Jimenez, C. J. Watts, J. Garatuza-Payan and W. J. Shuttleworth, 2004: Analysis of 2002 and 2003 warm-season precipitation from the North American monsoon experiment Event Rain Gauge Network. *Mon. Wea. Rev.*, **132**, 2938-2953.
- Gochis, D. J., J. C. Leal, W. J. Shuttleworth, C. J. Watts and J. Garatuza-Payan, 2003: Preliminary diagnostics from a new event-based precipitation monitoring system in support of the North American monsoon experiment. *J. Hydrometeorol.*, **4**, 974-981.
- Gochis, D.J., W.J. Shuttleworth and Z.-L. Yang 2002: Sensitivity of the modeled North American monsoon regional climate to convective parameterization. *Mon. Wea. Rev.*, **130**, 1282-1298.
- Gutzler, D. S., H. K. Kim, R. W. Higgins, H. M. H. Juang, M. Kanamitsu, K. Mitchell, K. Mo, P. Pegion, E. Ritchie, J. K. Schemm, S. Schubert, Y. Song and R. Yang, 2005: The North American Monsoon Model Assessment Project - Integrating numerical modeling into a field-based process study. *Bull. Am. Meteorol. Soc.*, **86**, 1423-1429.
- Harris, D., E. Foufoula-Georgiou and C. Kummerow, 2003: Effects of underrepresented hydrometeor variability and partial beam filling on microwave brightness temperatures for rainfall retrieval. *J. Geophys. Res.*, **108**, 8380.

- Higgins, W., D. Ahijevych, J. Amador, A. Barros, E. H. Berbery, E. Caetano, R. Carbone, P. Ciesielski, R. Cifelli and M. Cortez-Vazquez, 2006: The NAME 2004 Field Campaign and Modeling Strategy. *Bull. Am. Meteorol. Soc.*, **87**, 79-94.
- Hong, Y., K. Hsu, S. Sorooshian, and X. Gao. 2004: Precipitation Estimation from Remotely Sensed Imagery Using an Artificial Neural Network Cloud Classification System. *J. Appl. Meteor.*, **43**, 1834–1853.
- Hong, Y., K. L. Hsu, S. Sorooshian and X. G. Gao, 2005: Improved representation of diurnal variability of rainfall retrieved from the Tropical Rainfall Measurement Mission Microwave Imager adjusted Precipitation Estimation From Remotely Sensed Information Using Artificial Neural Networks (PERSIANN) system. *J. Geophys. Res.*, **110**, D06102, doi:10.1029/2004JD005301.
- Hong, Y., D. J. Gochis, Y. Cheng, K.-L. Hsu and S. Sorooshian, 2007: Evaluation of PERSIANN-CCS Rainfall Measurement using NAME Event Rain Gauge Network. *J. Hydrometeorol.*, **8**, 469-482.
- Hsu, K. L., X. G. Gao, S. Sorooshian and H. V. Gupta, 1997: Precipitation estimation from remotely sensed information using artificial neural networks. *J. Appl. Meteorol.*, **36**, 1176-1190.
- Huffman, G. J., R. F. Adler, D. T. Bolvin, G. Gu, E. J. Nelkin, K. P. Bowman, Y. Hong, E. F. Stocker and D. B. and Wolff, 2007: The TRMM Multi-satellite Precipitation Analysis: Quasi-Global, Multi-Year, Combined-Sensor Precipitation Estimates at Fine Scale. *J. Hydrometeorol.*, **8**, 38-55.

- Huffman, G. J., R. F. Adler, M. M. Morrissey, D. T. Bolvin, S. Curtis, R. Joyce, B. McGavock and J. Susskind, 2001: Global precipitation at one-degree daily resolution from multisatellite observations. *J. Hydrometeorol.*, **2**, 36-50.
- Janowiak, J. E., V. E. Kousky and R. J. Joyce, 2005: Diurnal cycle of precipitation determined from the CMORPH high spatial and temporal resolution global precipitation analyses. *J. Geophys. Res.*, **110**, D23105, doi:10.1029/2005JD006156..
- Janowiak, J. E., R. J. Joyce and Y. Yarosh, 2001: A real-time global half-hourly pixel-resolution infrared dataset and its applications. *Bull. Am. Meteorol. Soc.*, **82**, 205-217.
- Johnson, R. H., P. E. Ciesielski, B. D. McNoldy, P. J. Rogers and R. K. Taft, 2007: Multiscale Variability of the Flow During the North American Monsoon Experiment. *J. Climate*, **20**, 1628-1648.
- Joyce, R. J., J. E. Janowiak, P. A. Arkin and P. P. Xie, 2004: CMORPH: A method that produces global precipitation estimates from passive microwave and infrared data at high spatial and temporal resolution. *J. Hydrometeorol.*, **5**, 487-503.
- Kummerow, C., 1998: Beamfilling errors in passive microwave rainfall retrievals. *J. Appl. Meteorol.*, **37**, 356-370.
- Kummerow, C., Y. Hong, W. S. Olson, S. Yang, R. F. Adler, J. McCollum, R. Ferraro, G. Petty, D. B. Shin and T. T. Wilheit, 2001: The evolution of the Goddard profiling algorithm (GPROF) for rainfall estimation from passive microwave sensors. *J. Appl. Meteorol.*, **40**, 1801-1820.

- Lang, T. J., D. A. Ahijevych, S. W. Nesbitt, R. E. Carbone, S. A. Rutledge and R. Cifelli, 2007: Radar-Observed Characteristics of Precipitating Systems during NAME 2004. *J. Climate*, **20**, 1713-1733.
- Liu, C., E. J. Zipser and S. W. Nesbitt, 2007: Global distribution of Tropical deep convection: Different perspectives from TRMM infrared and radar data. *J. Climate*, **20**, 489-503.
- Mesinger F., Coauthors, 2006: North American Regional Reanalysis. *Bull. Amer. Meteor. Soc.*, **87**, 343–360.
- McCollum, J. R., W. F. Krajewski, R. R. Ferraro and M. B. Ba, 2002: Evaluation of biases of satellite rainfall estimation algorithms over the continental United States. *J. Appl. Meteorol.*, **41**, 1065-1080.
- Negri, A., R.F. Adler, E.J. Nelkin and G.J. Huffman, 1994: Regional rainfall climatologies derived from special sensor microwave (SSM/I) data. *Bull. Amer. Meteorol. Soc.*, **75**, 1165-1182.
- Nesbitt, S. W. and E. J. Zipser, 2003: The diurnal cycle of rainfall and convective intensity according to three years of TRMM measurements. *J. Climate*, **16**, 1456-1475.
- Nesbitt, S. W., E. J. Zipser and C. D. Kummerow, 2004: An examination of version-5 rainfall estimates from the TRMM Microwave Imager, precipitation radar, and rain gauges on global, regional, and storm scales. *J. Appl. Meteorol.*, **43**, 1016-1036.
- Rosenfeld, D., and C. W. Ulbrich, 2003: Cloud microphysical properties, processes, and rainfall estimation opportunities. *Meteor. Monogr.*, **30**, 237-258.

- Rowe, A. K., S. A. Rutledge, T. J. Lang, P. E. Ciesielski, and S. M. Saleeby, 2008: Elevation-dependent trends in precipitation during NAME. *Mon. Wea. Rev.*, submitted.
- Saleeby, S. M. and W. R. Cotton, 2004: Simulations of the North American Monsoon System. Part I: Model analysis of the 1993 monsoon season. *J. Climate*, **17** 1997-2018.
- Smith, J. A. and W. F. Krajewski, 1991: Estimation of the mean field bias of radar estimates. *J. Appl. Meteorol.*, **30**, 397-412.
- Sorooshian, S., K. L. Hsu, X. Gao, H. V. Gupta, B. Imam and D. Braithwaite, 2000: Evaluation of PERSIANN system satellite-based estimates of tropical rainfall. *Bull. Am. Meteorol. Soc.*, **81**, 2035-2046.
- Steiner, M., and J.A. Smith, 2004: Scale dependence of radar-rainfall rates—An assessment based on raindrop spectra. *J. Hydrometeorol.*, **5**, 1171–1180.
- Stensrud, D. J., R. L. Gall and M. K. Nordquist, 1997: Surges over the Gulf of California during the Mexican Monsoon. *Mon. Weather Rev.*, **125**, 417-437.
- Stull, R.B. 1995: *Meteorology today: For scientists and engineers*. West Publishing Company, St. Paul, MN, pg. 88.
- Tripoli, G. J., and W. R. Cotton, 1989a: Numerical study of an observed orogenic mesoscale convective system. Part I: Simulated genesis and comparison with observations. *Mon. Wea. Rev.*, **117**, 273–304.
- Tripoli, G. J., and W. R. Cotton, 1989b: Numerical study of an observed orogenic mesoscale

- convective system. Part II: Analysis of governing dynamics. *Mon. Wea. Rev.*, **117**, 305–328.
- Tustison, B., D., Harris, E. Foufoula-Georgiou, 2001: Scale issues in verification of precipitation forecasts. *J. Geophys. Res.*, **106**, 11775-11784.
- Tustison, B., D., E. Foufoula-Georgiou, and D. Harris, 2003: Scale-recursive estimation for multisensor quantitative precipitation forecast verification: A preliminary assessment. *J. Geophys. Res.*, **107**, 8377, doi:10.1029/2001JD001073.
- Vivoni, E.R., H.A. Guitierrez-Jurado, C.A. Aragon, L.A. Mendez-Barrozo, A.J. Rinehart, R.L. Wyckoff, J.C. Rodriguez, C.J. Watts, J.D. Bolten, V. Lakshmi, and T.J. Jackson, 2007: Variation of hydrometeorological conditions along a topographic transect in northwestern Mexico during the North American monsoon. *J. Climate*, **20**, 1792-1809.
- Whiteman, C. D., 2000: *Mountain Meteorology: Fundamentals and Applications*. Oxford University Press, 355 pp.
- Xie, P. P. and P. A. Arkin, 1997: Global precipitation: A 17-year monthly analysis based on gauge observations, satellite estimates, and numerical model outputs. *Bull. Am. Meteorol. Soc.*, **78**, 2539-2558.
- Xie, P., Y. Yarosh, M. Chen, R. Joyce, J. J. Janowiak, and P. A. Arkin, 2005: Diurnal cycle of cloud and precipitation associated with the North America monsoon system: Preliminary results for 2003 and 2004. *Preprints*, 16th Conference on Climate Variability and Change, 85th Annual Amer. Meteor. Soc. Meeting, San Diego, CA, Amer. Meteor. Soc.

Table Caption

Table 1. For each precipitation estimate, fraction of variance explained by the mean diurnal cycle in each elevation band.

Figure Captions

Fig. 1. (a) Map showing the region of study, including terrain elevation (shaded, m), the location of ground-based scanning radars (\diamond) and 210 km range rings from each radar, as well as the locations of NERN gauges (+). Mean 1998-2004 3B42 July-August precipitation is contoured with the thick lines. (b) Map showing the location of 0.25° grids used in this study, shaded by elevation band.

Fig. 2. Time series of mean precipitation rate ($\text{mm dy}^{-1} \text{ 3hr}^{-1}$) for the period 00 UTC 1 June through 21 UTC 31 August 2004 for the 5 precipitation estimates for 0.25° grid points above 2250 m (top panel), between 500 m and 2250 m (middle panel), and below 500 m (bottom panel).

Fig. 3. Time series of (a) mean diurnal precipitation rate ($\text{mm dy}^{-1} \text{ 3hr}^{-1}$) and (b) mean diurnal precipitation frequency for the period 00 UTC 1 June through 21 UTC 31 August 2004 for the 5 precipitation estimates for 0.25° grid points above 2250 m (top panel), between 500 m and 2250 m (middle panel), and below 500 m (bottom panel).

Fig. 4. Each panel shows a map of shaded frequency of precipitation (expressed as percent) according to the NAME version 2 CSU/NCAR radar composites, as well as the frequency of precipitation according to the NERN gauges (filled circles) over each hour beginning at the time labeled on each panel. White areas indicate no radar data was collected in this region.

Fig. 5. Each panel shows a map of shaded relative frequency of IR brightness temperatures less than 275 K, as well as the contoured frequency of IR brightness temperatures less than 208 K (between 0 and 20% by 4% increments) every 2 hours for satellite observations during the hour beginning at the time labeled on each panel. The dark grey and black lines indicate the coastline and 2250 m elevation contours, respectively.

Fig. 6. Shaded frequency diagrams of the relative fraction of IR brightness temperature counts (only for observations ≤ 275 K) in 5 K brightness temperature bins as a function of each hour local time.

Fig. 7. Time series of IR brightness temperatures (shaded, greyscale) and radar reflectivity (shaded, colors) for the period 12 LT 2 August 2004 to 16 LT 3 August 2004. The nominal range of the NAME radars is indicated at upper left. The arrows indicate the location of inferred nocturnal stratus clouds.

Fig. 8. For surface stations at Ciénega de Nuestra Señora, El Palmito, Mazatlán, and Culiacán, mean diurnal time series of (a) temperature ($^{\circ}\text{C}$, solid), relative humidity (%), dashed), and (b) estimated cloud base height (km).

Fig. 9. Schematic of observed diurnal mechanisms along the SMO at 25°N . Cloud type indicates relative height attained by clouds, shading indicates specific (not relative) humidity contrasts, asterisks (*) indicate mixed-phase microphysical processes, and density of vertical streaks indicate the location and relative intensity of precipitation.

Table 1. For each precipitation estimate, fraction of variance explained by the mean diurnal cycle in each elevation band.

Band	NERN	Radar	CMORPH	PERSIANN	3B42
Elevation \geq 2250 m	0.37	0.32	0.36	0.31	0.38
500 m \leq elevation < 2250 m	0.32	0.13	0.27	0.29	0.31
Elevation < 500 m	0.22	0.18	0.16	0.23	0.15

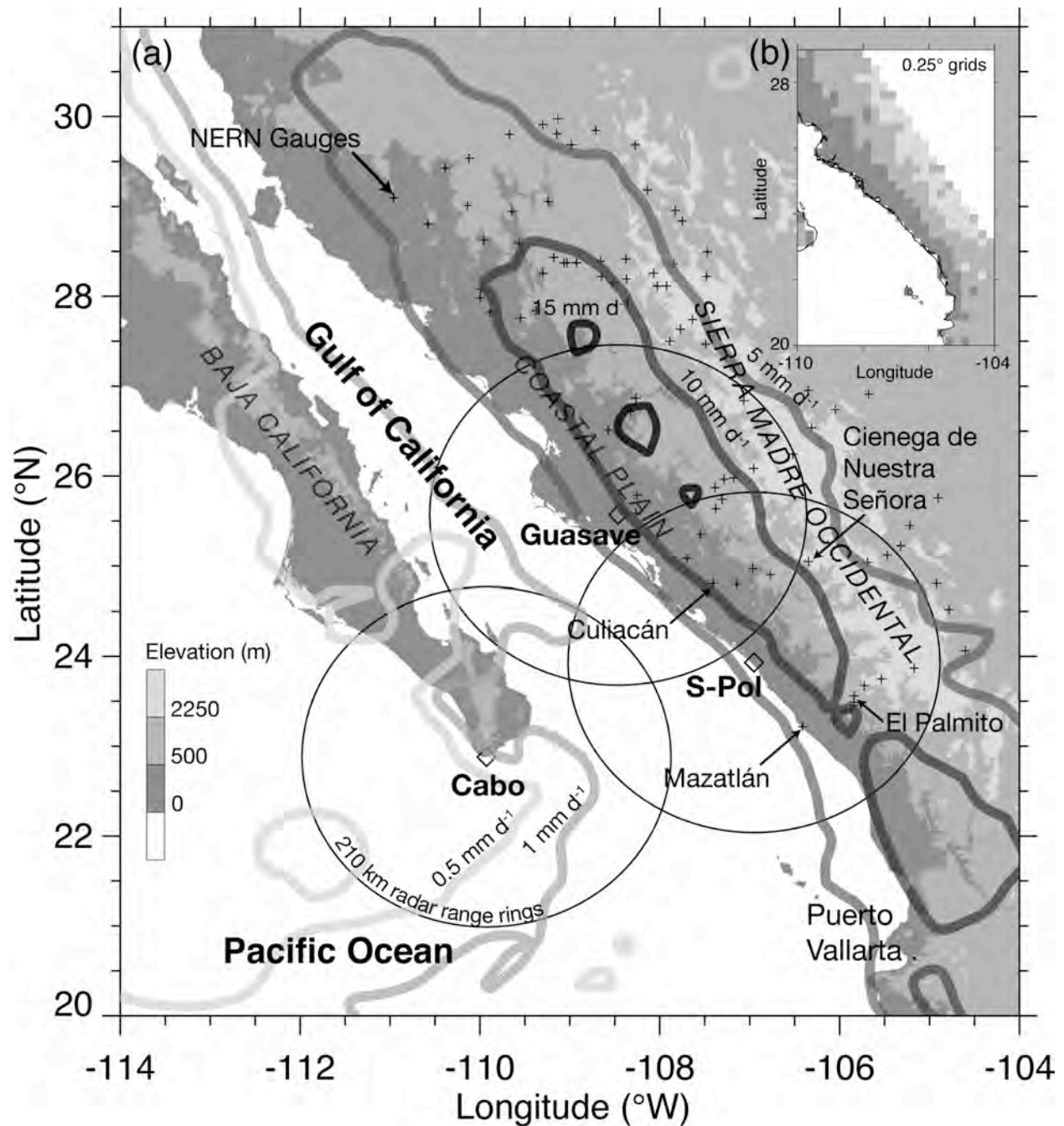


Fig. 1. (a) Map showing the region of study, including terrain elevation (shaded, m), the location of ground-based scanning radars (\diamond) and 210 km range rings from each radar, as well as the locations of NERN gauges (+). Mean 1998-2004 3B42 July-August precipitation is contoured with the thick lines. (b) Map showing the location of 0.25° grids used in this study, shaded by elevation band.

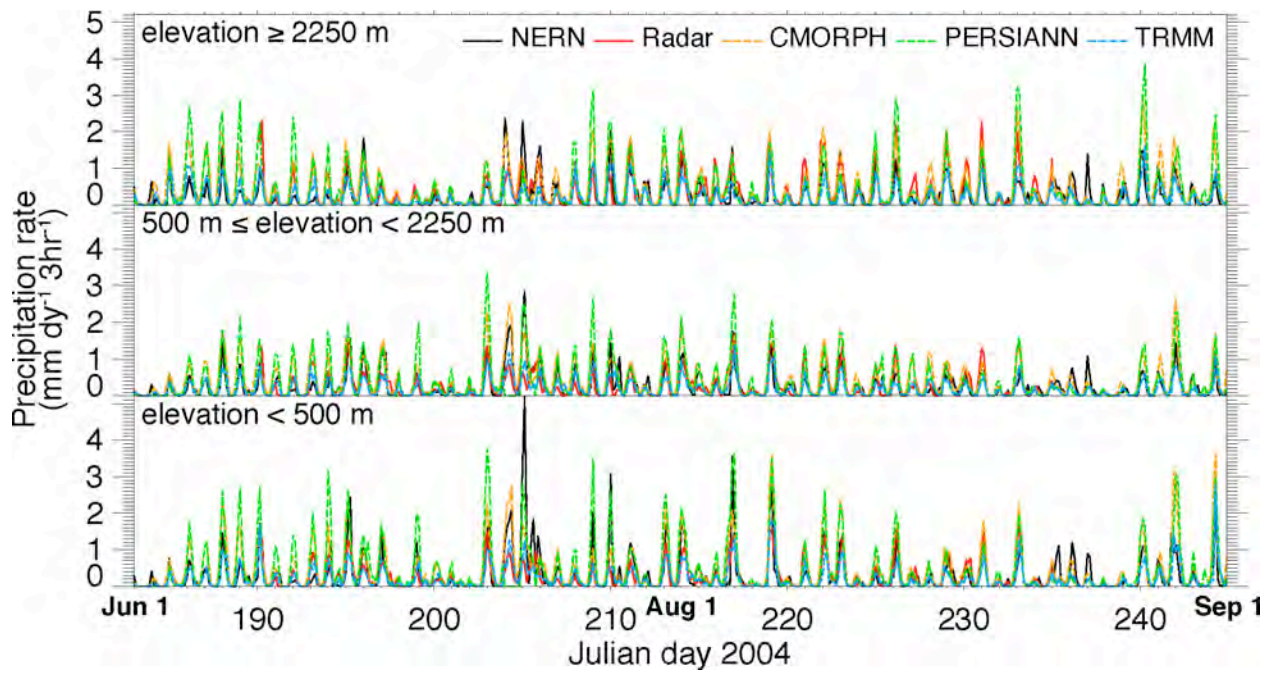


Fig. 2. Time series of mean precipitation rate ($\text{mm dy}^{-1} \text{ 3hr}^{-1}$) for the period 00 UTC 1 June through 21 UTC 31 August 2004 for the 5 precipitation estimates for 0.25° grid points above 2250 m (top panel), between 500 m and 2250 m (middle panel), and below 500 m (bottom panel).

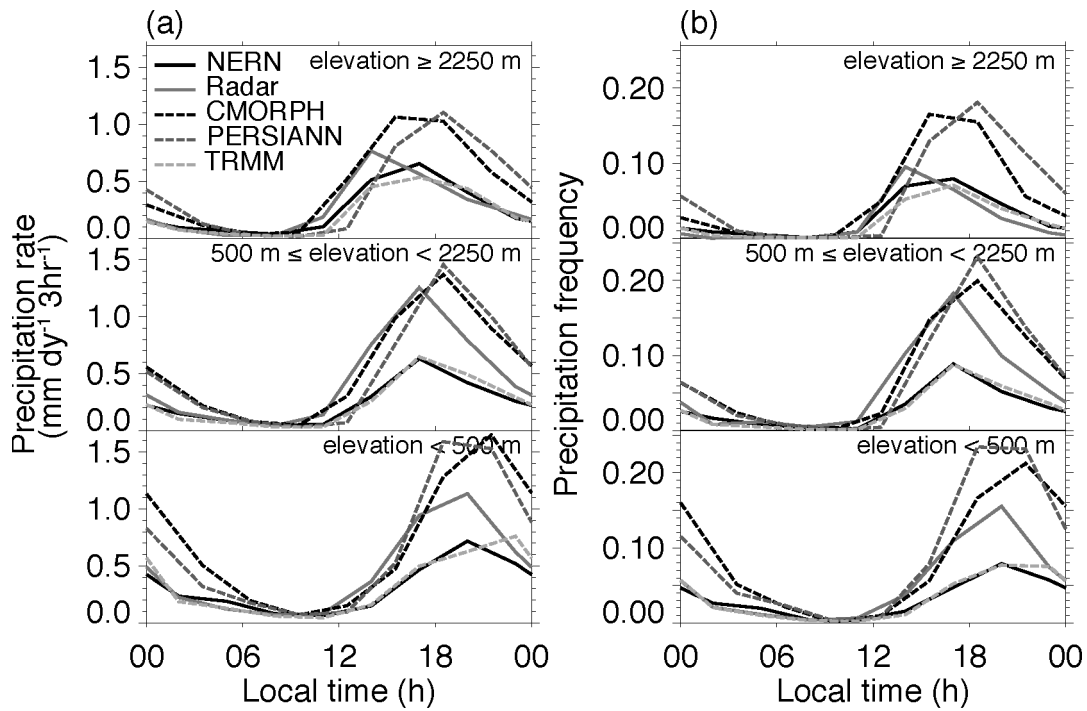


Fig. 3. Time series of (a) mean diurnal precipitation rate ($\text{mm dy}^{-1} 3\text{hr}^{-1}$) and (b) mean diurnal precipitation frequency for the period 00 UTC 1 June through 21 UTC 31 August 2004 for the 5 precipitation estimates for 0.25° grid points above 2250 m (top panel), between 500 m and 2250 m (middle panel), and below 500 m (bottom panel).

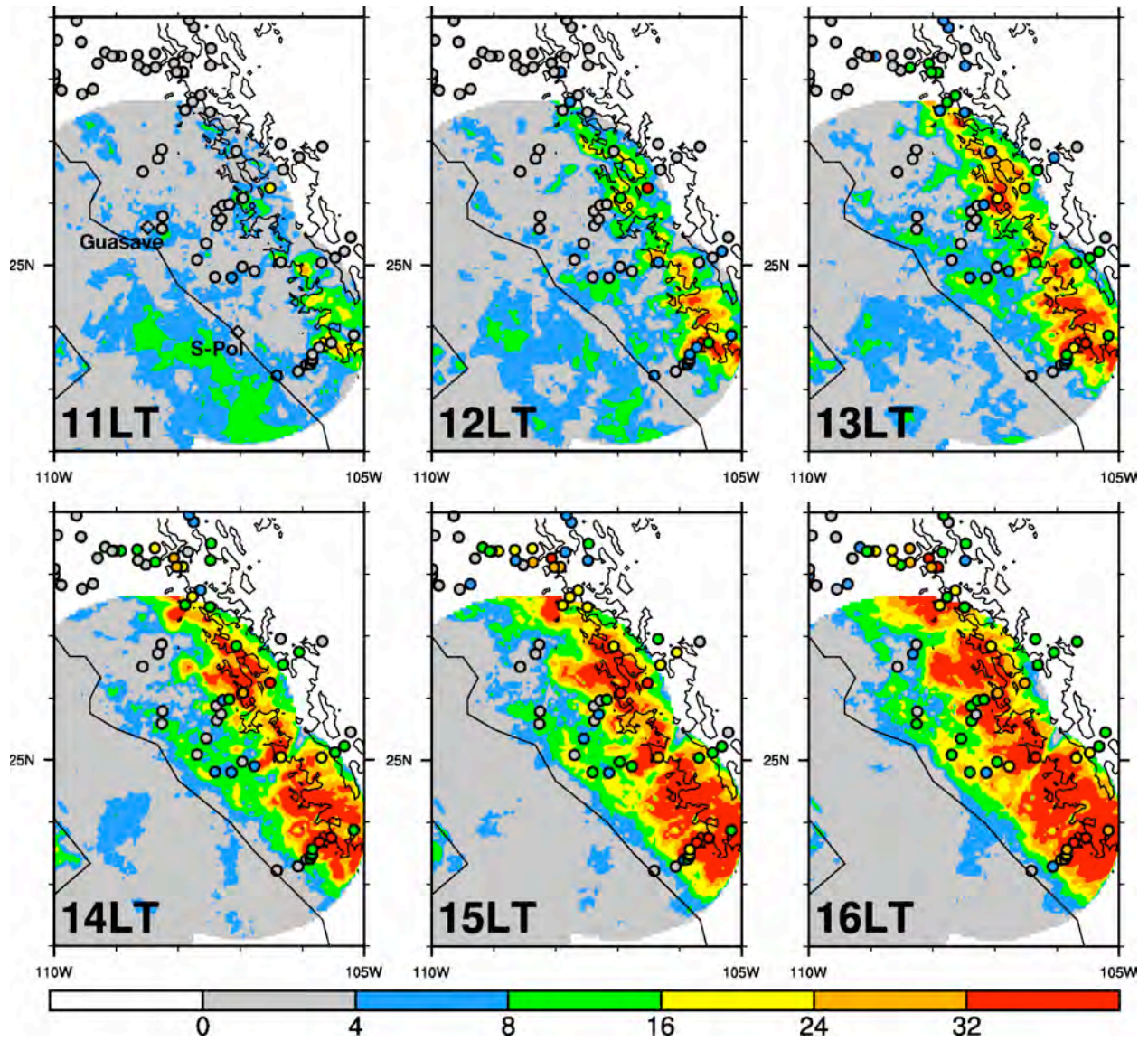


Fig. 4. Each panel shows a map of shaded frequency of precipitation (expressed as percent) according to the NAME version 2 CSU/NCAR radar composites, as well as the frequency of precipitation according to the NERN gauges (filled circles) over each hour beginning at the time labeled on each panel. White areas indicate no radar data was collected in this region.

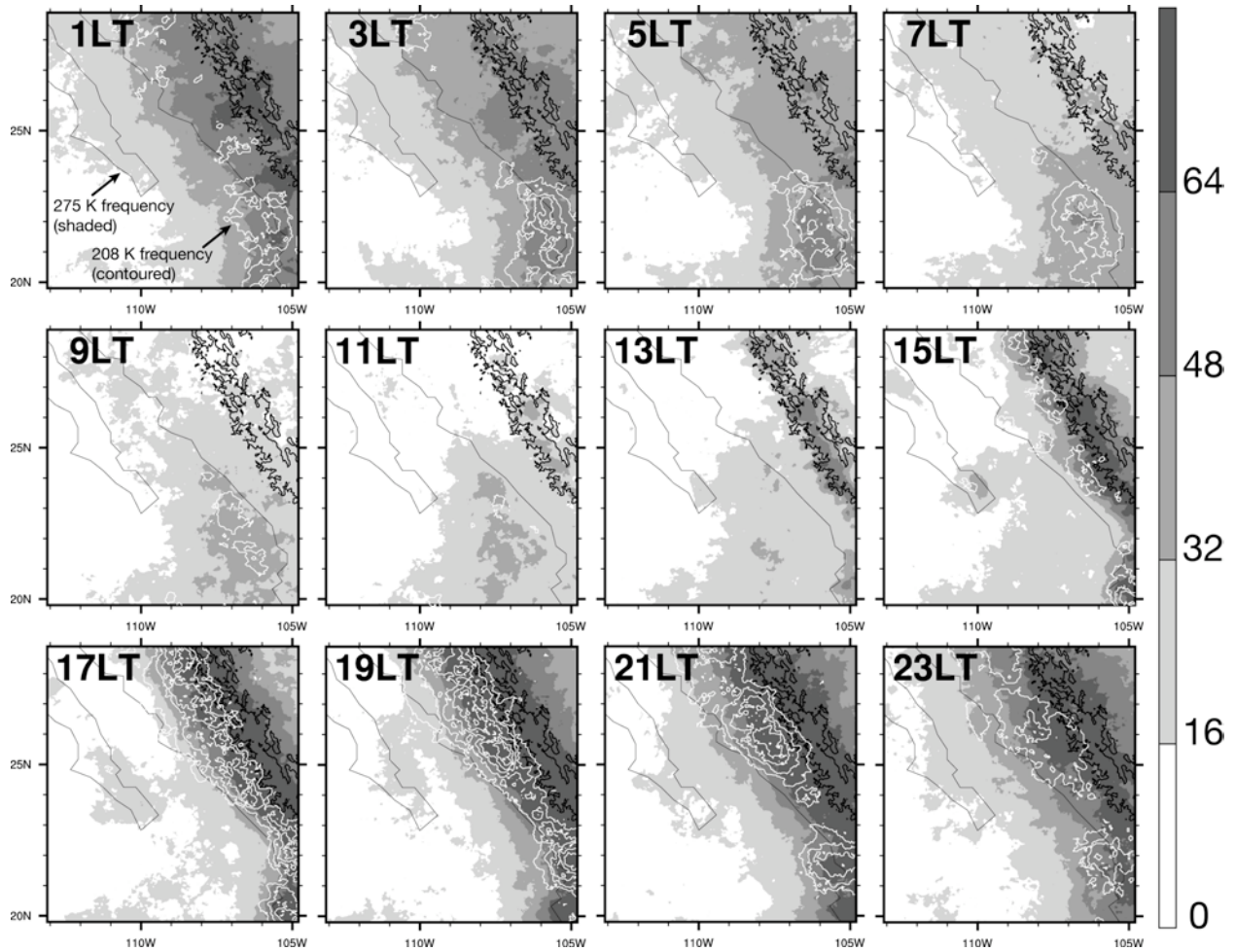


Fig. 5. Each panel shows a map of shaded relative frequency of IR brightness temperatures less than 275 K, as well as the contoured frequency of IR brightness temperatures less than 208 K (between 0 and 20% by 4% increments) every 2 hours for satellite observations during the hour beginning at the time labeled on each panel. The dark grey and black lines indicate the coastline and 2250 m elevation contours, respectively.

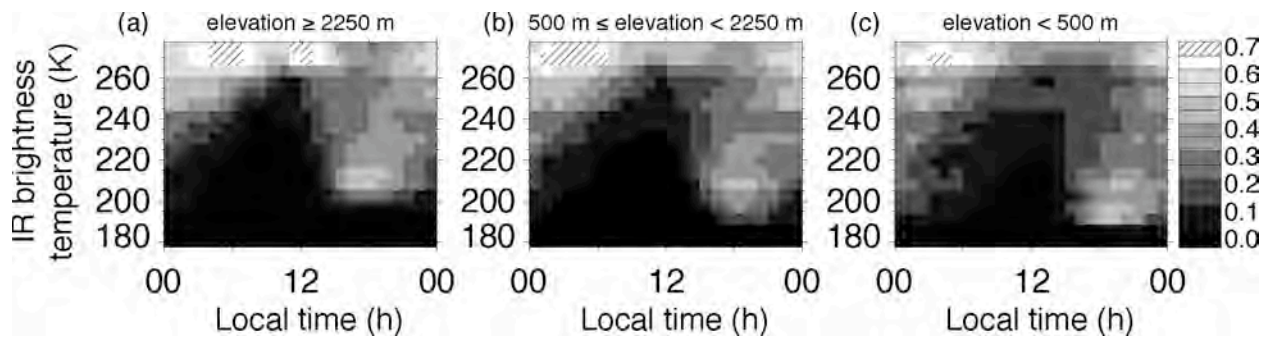


Fig. 6. Shaded frequency diagrams of the relative fraction of IR brightness temperature counts (only for observations ≤ 275 K) in 5 K brightness temperature bins as a function of each hour local time.

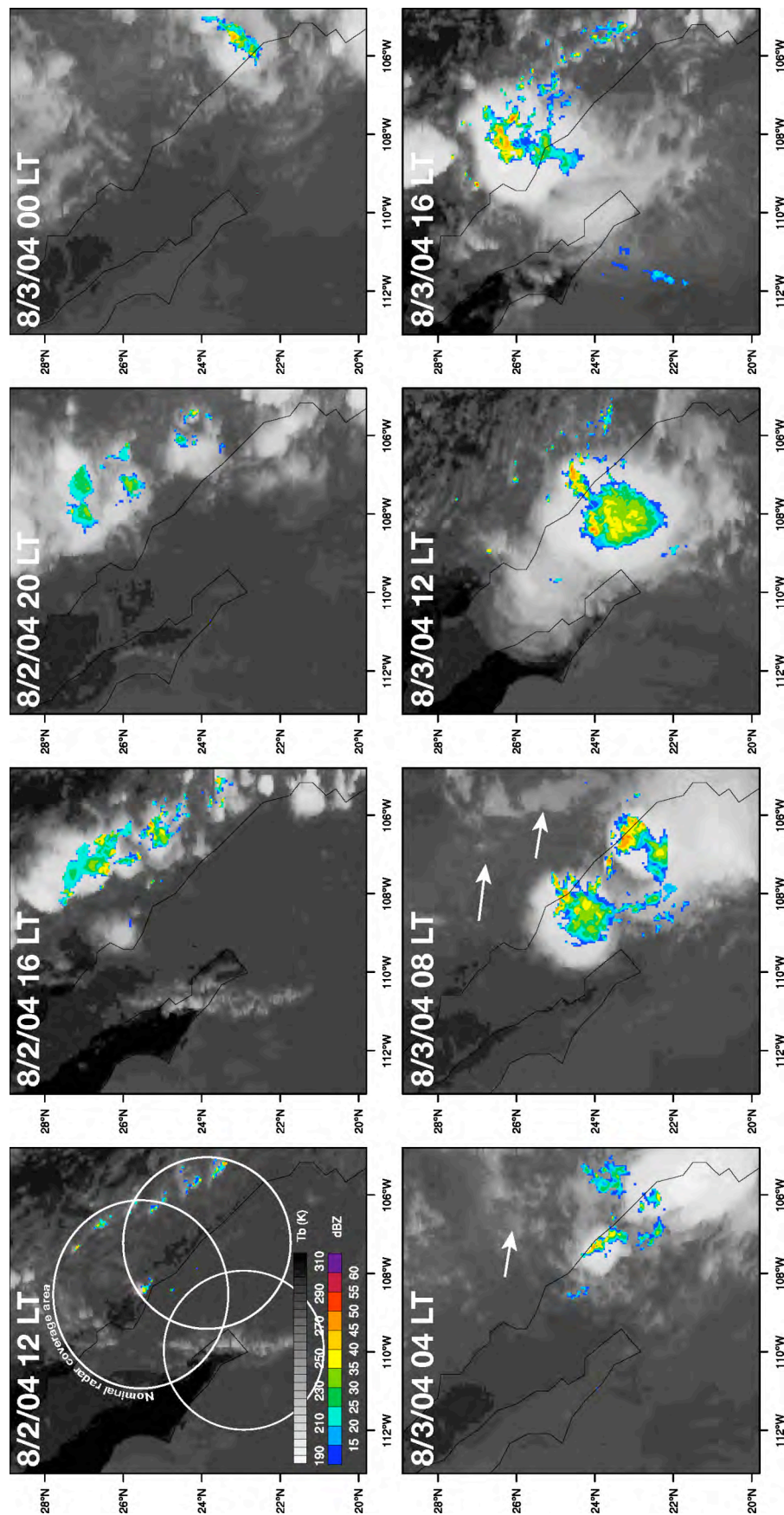


Fig. 7. Time series of IR brightness temperatures (shaded, greyscale) and radar reflectivity (shaded, colors) for the period 12 LT 2 August 2004 to 16 LT 3 August 2004. The nominal range of the NAME radars is indicated at upper left. The arrows indicate the location of inferred nocturnal stratus clouds.

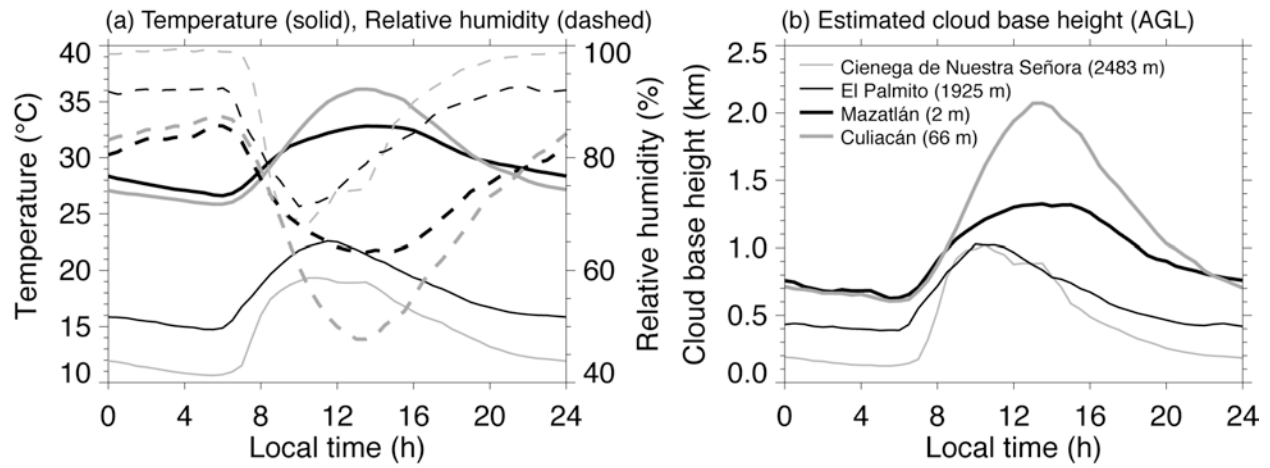


Fig. 8. For surface stations at Cienega de Nuestra Señora, El Palmito, Mazatlán, and Culiacán, mean diurnal time series of (a) temperature (°C, solid), relative humidity (%), and (b) estimated cloud base height (km).

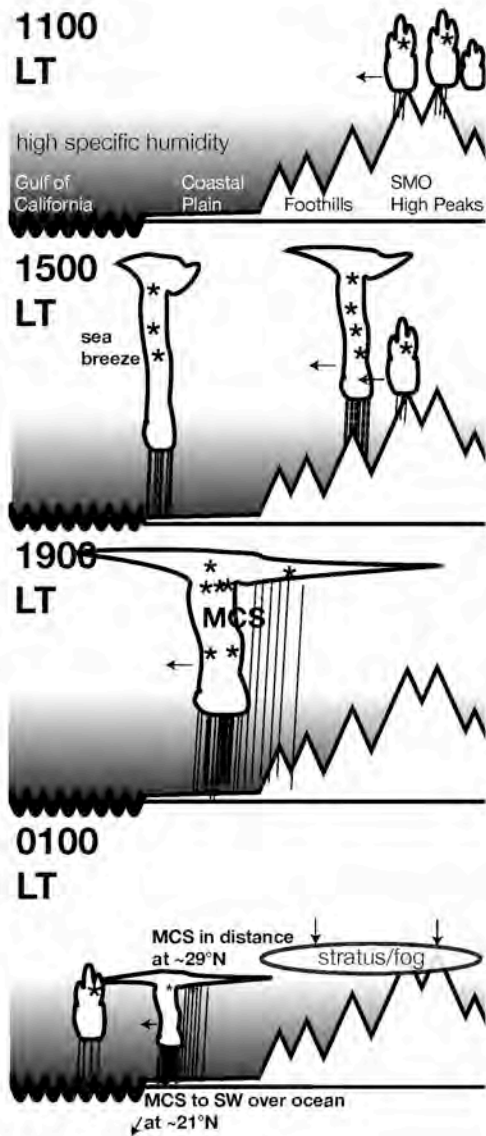


Fig. 9. Schematic of observed diurnal mechanisms along the SMO at 25°N. Cloud type indicates relative height attained by clouds, shading indicates specific (not relative) humidity contrasts, asterisks (*) indicate mixed-phase microphysical processes, and density of vertical streaks indicate the location and relative intensity of precipitation.